Multidimensional imbalances in cortical circuit activity in Fragile-X Syndrome mice

Cian O'Donnell[1,2,*], J. Tiago Gonçalves[3,4], Carlos Portera-Cailliau[3] and Terrence J. Sejnowski[2,5,*]

[1]Department of Computer Science, University of Bristol, Bristol, UK

[2]Howard Hughes Medical Institute, Salk Institute for Biological Studies, La Jolla CA, USA

[3]Departments of Neurology and Neurobiology, David Geffen School of Medicine at UCLA, Los Angeles, CA, USA

[4]Dominick Purpura Department of Neuroscience, Albert Einstein College of Medicine, Bronx, NY, USA

[5]Division of Biological Sciences, University of California at San Diego, La Jolla, CA, USA

*Correspondence: cian.odonnell@bristol.ac.uk (C.O'D.), terry@salk.edu (T.J.S.)

Abstract

A leading theory for multiple neurodevelopmental brain disorders holds that they arise from imbalances in excitatory and inhibitory (E/I) brain circuitry. However this theory has rarely been quantitatively tested. Here we combined computational modeling and analysis of *in vivo* 2-photon Ca^{2+} imaging data from cortex of wild-type and *Fmr1* knock-out (KO) mice to test the E/I imbalance model. Our main findings were: 1) the E/I imbalance model was not rich enough to capture the alterations in neural activity statistics in *Fmr1* KO mice; 2) greatly varying effects of synaptic and cellular properties on network activity; 3) opposite changes in circuit properties of *Fmr1* KO mice at different stages of development; 4) a reduction in the entropy of circuit activity in young *Fmr1* KO mice, but an opposite increase in adult *Fmr1* KO mice. These findings suggest qualitatively new strategies for understanding circuit alterations in Fragile-X Syndrome and related disorders.

Introduction

The nervous system shows complex organization at many spatial scales: from genes and molecules, to cells and synapses, to neural circuits. Ultimately, the electrical and chemical signaling at all of these levels must give rise to the behavioral and cognitive processes seen at the whole-organism level. When trying to understand prevalent brain disorders such as Autism and Schizophrenia, a natural question to ask is: where does the most productive level of neuroscientific investigation lie? Traditionally, most major disorders are diagnosed entirely at the behavioral level, whereas pharmaceutical interventions are targeted at correcting alterations at the molecular level. Even for the most successful drugs, we have little understanding of how these pharmaceutical actions at the molecular level percolate up the organizational ladder to affect behavior and cognition. This classic bottom-up approach may even be further confounded if phenotypic heterogeneity in Autism turns out not to reflect a unique cellular pathology, but rather a perturbation of network properties when neurons interact (Belmonte et al., 2004). These considerations imply that a more promising level of analysis might be at the level of neural circuits, for two reasons. First, circuits are closer to the behavioral level than the molecular signaling of cells is; therefore, it might be easier to predict how interventions at the circuit level affect behavior. Second, since we have fewer neurons than molecules and fewer neural circuits than neurons, the dimensionality of the brain's neural circuit properties is likely much smaller than that of the brain's molecular properties. It might turn out to be easier to find interventions that push circuit-level properties of brain disorder patients towards the operating regimes observed in healthy subjects, than it would be to correct the corresponding deficits in patients at the molecular level.

One prominent circuit-level hypothesis for brain disorders has been the idea of an imbalance in excitatory and inhibitory signaling. First proposed as a model for Autism (Rubenstein and Merzenich, 2003), the concept has since been applied to many other brain disorders, including Schizophrenia, Rett Syndrome, Fragile-X Syndrome, Tuberous Sclerosis, and Angelman Syndrome (Bateup et al., 2011; Dani et al., 2005; Gibson et al., 2008; Kehrer et al., 2008; Wallace et al., 2012). However, a major drawback of this model in its simplest form is that it is entirely 1-dimensional. It implies that either too much excitation or too much inhibition is

unhealthy, and by extension that the symptoms of these disorders could be normalized by either enhancing or reducing the level of, say, GABAergic signaling as appropriate. Although clinical trials for such GABAergic-based interventions are ongoing (Braat and Kooy, 2015), no treatment for a neurodevelopmental disorder based on this principle has yet been validated.

In this study we compare *in vivo* neocortical circuit activity data recorded from wild-type and Fragile-X model mice, and find that the classic 1-dimensional E/I imbalance model is not flexible enough to capture the observed differences. Instead, we argue that higher-dimensional models are needed. We demonstrate that a novel 2D neural circuit model can account for many of the differences in circuit activity that are likely important for neural coding and information processing. Finally, we apply a recently developed large-scale data analysis method (O'Donnell et al., 2017) to our Ca^{2+} imaging data to uncover systematic shifts in neural circuit activity pattern properties across development in Fragile-X.

Results

Neural circuits consist of many components, connected together in a seemingly complicated fashion. These components typically interact non-linearly to generate circuit activity dynamics. Although many properties of cortical circuit components have been found to be altered in animal models of brain disorders, it remains extremely difficult to predict the net effect of varying any one particular parameter on circuit behavior.

To explore this issue more concretely, we built a computational model of layer (L) 2/3 mouse somatosensory cortex. This circuit has been studied in detail by neurophysiologists, and several of its properties have been found to be altered during development in mouse models of Fragile-X syndrome, including parvalbumin-positive interneuron number (Selby et al., 2007), GABA receptor reversal potential (He et al., 2014), dendritic spine dynamics (Cruz-Martin et al., 2010), and L4 excitatory input (Bureau et al., 2008), reviewed by (Contractor et al., 2015). In the ideal case we would like to derive a mathematical relationship between any arbitrary circuit parameter and its effect on circuit function, but for even reasonably complicated models this problem quickly becomes analytically intractable. Because of this difficulty, we used numerical computer simulations to perform hypothetical experiments where we perturbed various parameters of the circuit model and observed the resulting changes in circuit-level activity. Although we focus on this particular circuit for tractability, our general conclusions and methodology should be readily applicable to other brain circuits (Frye and Maclean, 2016).

The L2/3 computational model we built (Figure 1A, see Methods for details) consisted of four interconnected populations of leaky integrate-and-fire neurons: one group of 1700 excitatory (E) pyramidal neurons and three groups of inhibitory neurons: 115 $5HT_{3A}$R-expressing neurons, 70 parvalbumin-expressing (PV) neurons, and 45 somatostatin-expressing (SOM) neurons. This L2/3 circuit was driven by a separate population of 1500 L4 excitatory neurons. Cellular numbers, intrinsic properties, synaptic strengths, and connectivity statistics were taken from published *in vitro* data from P17—22 wild-type mice (Avermann et al., 2012; Lefort et al., 2009; Tomm et al., 2014).

L2/3 neurons of the rodent somatosensory neocortex respond only sparsely to sensory stimulation *in vivo*. For example, twitching a whisker activates, on average, only ~20% of neurons in its corresponding barrel, each of which typically emits only one action potential (Clancy et al., 2015; Kerr et al., 2007; Sato et al., 2007). Hence any individual neuron carries very little information about the stimulus on its own, implying that information must instead be encoded at the circuit level as the identities of the subset of neurons that respond.

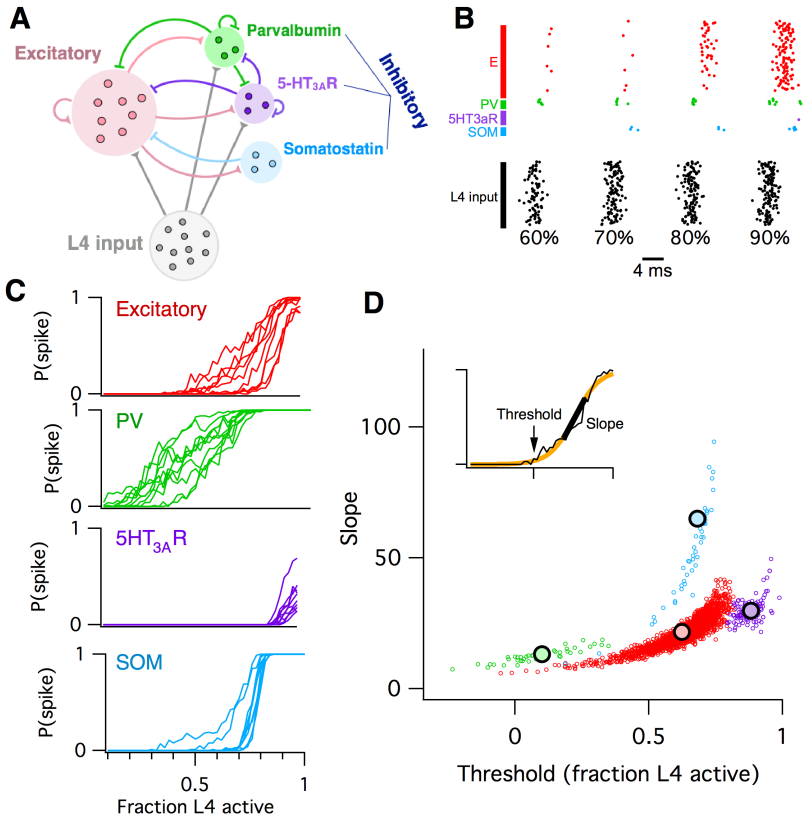

Figure 1. Computational model of L2/3 mouse somatosensory cortex.
A: Schematic diagram of computational circuit model.
B: Example raster plots of spiking responses from a subset of neurons from each cell type (colors as in panel A), for varying fractions of L4 activated (black).
C: Probability of spiking as a function of the fraction of L4 neurons activated. Each curve represents the response probability of a single neuron, averaged over multiple trials and multiple permutations of active L4 cells.
D: Each circle plots the fitted logistic slope and threshold values for a single neuron in the simulation. Circle color indicates cell type: red is excitatory, green is PV inhibitory, purple is 5ht3AR inhibitory, blue is SOM inhibitory. Large black circles indicate mean for each cell-type. Inset shows an example fitted logistic response function (orange) to the noisy simulation results from a single excitatory neuron (black).

To model whisker stimulation, we simulated a volley of spikes arriving from L4 as input to the population of L2/3 cells. We chose a random subset of L4 neurons as ON, then sent a single spike from each of these L4 cells to their target neurons in L2/3, and recorded the responses of all neurons in L2/3, some of which spiked and some of which did not. We repeated this identical stimulation multiple times, in order to get an average response probability for each L2/3 neuron, given the probabilistic vesicle release at synapses in the model. Then we chose a different random subset of L4 neurons as ON, and repeated the entire procedure. Finally, we varied the fraction of L4 cells active and plotted the probability of response for each individual L2/3 neuron as a function of L4 activity level (Figure 1B—C).

We found that the mean response probability of each neuron in the simulation increased from zero to one monotonically with increasing L4 activity level. Neurons of all four cell types responded to the L4 stimulus, including the SOM interneurons which did not receive direct L4 input, but were instead excited by disynaptic connections via L2/3 excitatory neurons. The shape of the response curve varied systematically across cell types, and was heterogeneous for different neurons of a given cell type. To quantify these differences, we used logistic regression to fit the response profile of each neuron with a sigmoid function (Figure 1D, inset), which has just two parameters: the slope (representing the steepness of the response curve) and threshold (representing the minimal fraction of L4 neurons needed to activate the cell). When we plotted the fitted slope and threshold values for each neuron against each other, we found that each cell type falls into a distinct cluster in this 2-dimensional space. For example, all PV inhibitory neurons had a low slope and low threshold, whereas SOM inhibitory neurons had a steep slope and moderate threshold. We will use these slope-threshold measurements to summarize the circuit-level input-output function of this 'default' model of L2/3 somatosensory cortex.

The circuit model contains 100 parameters (Materials and Methods), several of which are altered in Fragile-X mouse models. How sensitive is the circuit's macroscopic input-output function to alterations in its low-level components? To test this, we varied 76 of the model parameters in turn by ±20%, and repeated the entire set of simulations for each case (Materials and Methods). For each individual parameter alteration, we fit a new logistic

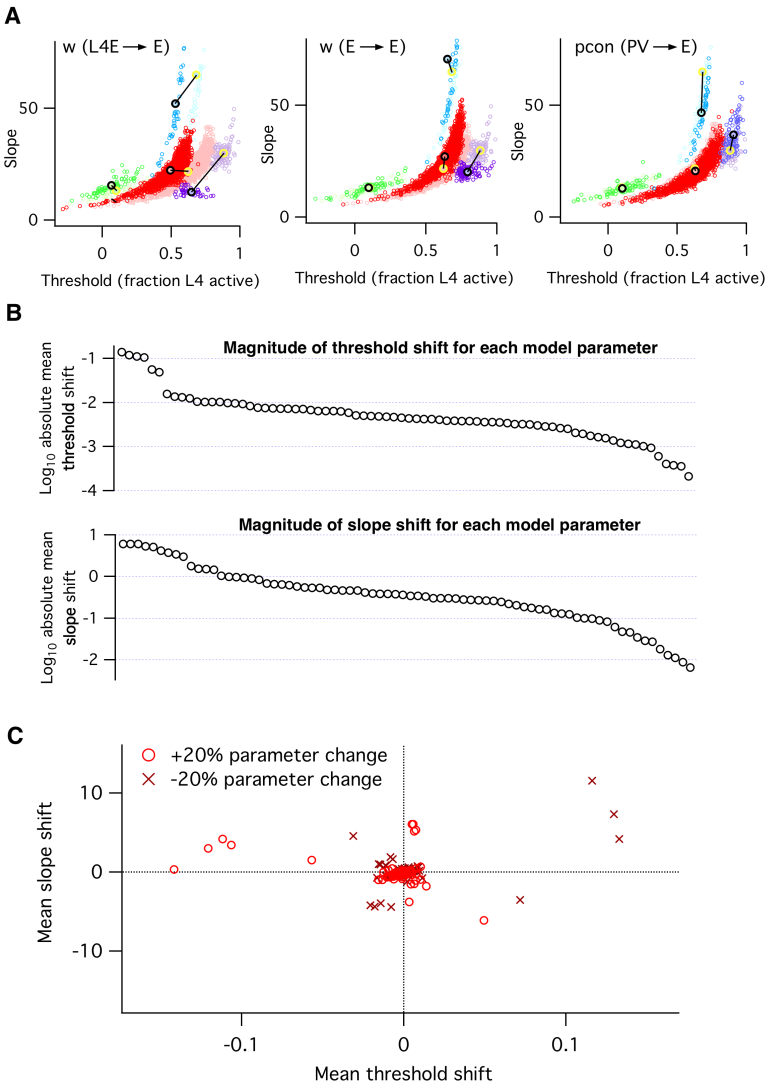

Figure 2. Heterogeneous effects of varying L2/3 parameters on the circuit input-output function.

A: Shifts in the distribution of fitted slope and threshold parameters as a result of increasing the strength of synapses from L4 to L2/3 E neurons (left), increasing the strength of recurrent synapses between L2/3 E neurons (center), or increasing the connection probability between L2/3 PV interneurons and E neurons (right). Transparent circles represent values for default network, heavy circles for altered network. The four colors represent different cell types, as in Figure 1. The default and altered group means are large yellow and black open circles, respectively.

B: Absolute values of mean shifts in threshold (upper plot) and slope (lower plot) for E neurons arising from increasing the value of each parameter by +20%. Note that data are presented on a log10 scale.

C: The shift in mean slope-threshold parameter values for E neurons from the default network values, in response to each of the 59 circuit parameter alterations. Light red circles indicate +20% increase in parameter value; dark red crosses indicate a -20% decrease in parameter value.

response function for each model neuron. We summarize the results by plotting the logistic slope and threshold parameters and comparing their values to those found with the default model. The outcomes were hugely varied. We show three examples from the set of fifty-nine in Figure 2A, chosen to illustrate three qualitatively different effects that neural parameter changes can have on circuit function. First, when we increased the amplitude of postsynaptic potentials (PSPs) of excitatory synapses from L4 to L2/3 excitatory neurons, we found that the logistic threshold parameter of all cell types shifted leftwards to lower values (Figure 2A left), implying that fewer L4 neurons were needed to activate the entire L2/3 circuit. In contrast, when we increased the PSP amplitude of a different excitatory synapse, the recurrent connections between L2/3 excitatory neurons, we found (Figure 2A center) that excitatory and SOM inhibitory neurons had increased slope parameters relative to default, with little change in their threshold parameters. $5HT_{3A}R$ inhibitory neurons had decreased slopes and thresholds, while PV neurons had little change at all. As a third example we increased the probability of inhibitory synaptic connections from L2/3 PV interneurons to L2/3 excitatory neurons (Figure 2A right). In this case we found that excitatory neurons had a lower slope and increased threshold, SOM inhibitory neurons had a lower slope, $5HT_{3A}R$ inhibitory neurons had both an increased slope and threshold, and PV neurons showed little change, even though their outgoing synapses were the parameter that was altered.

To synthesize the findings from all simulations, for each altered parameter we plotted the shift in mean slope-threshold values for L2/3 excitatory neurons from the mean values found with the default model (Figure 2B). We focused on excitatory neurons because they constitute 90% of the neurons in this layer (Lefort et al., 2009) and are the primary output to downstream circuits (Mao et al., 2011; Petreanu et al., 2007). Overall, we found a very heterogeneous picture. First, the magnitude of the shift in circuit response varied dramatically from parameter to parameter (Figure 2B—C). Varying some parameters, such as the first two examples given above, had large effects, whereas varying other parameters such as w_{l5htE} (the strength of synapses from $5HT_{3A}R$ inhibitory neurons to E neurons) or τm_{lsom} (the membrane time constant of SOM inhibitory neurons) had little effect. Second, the direction of shift in 2-D slope-threshold space also depended on parameter (Figure 2C). Increasing some parameters

changed either circuit slope or threshold in isolation, while other parameters changed both slope and threshold together. All four quadrants of the slope-threshold plane could be reached by various subsets of the model parameters. Third, basic knowledge of whether a component was 'excitatory' or 'inhibitory' was insufficient to predict the direction of slope-threshold change. For example, the two glutamatergic projections considered in Figure 2A had distinct effects on circuit function.

In summary, these simulations indicate that the L2/3 somatosensory cortex circuit has extremely varied sensitivities to changes in its cellular components, and that the eventual circuit-level consequences cannot be predicted from knowledge of the class of the perturbed neurotransmitter alone.

Firing rates and correlations from the logistic model

Above we investigated how low-level circuit components affect a high-level circuit input-output function, as parameterized by the slope and threshold of fitted logistic functions. But how is this logistic input-output function related to more common measures of neural population activity, such as firing rates and pairwise correlations between neurons? To investigate this, we considered the following reduced statistical model of cortical activity. We assumed for simplicity that the magnitude of the total input to the L2/3 circuit is a Gaussian distributed random variable, with zero mean and unit standard deviation (Figure 3A lower left). Then we described each L2/3 neuron's input-output as a logistic function as before (Figure 3A upper left), with threshold and slope defined relative to the Gaussian input's mean and standard deviation, respectively. Given this model, we can numerically calculate the probability distribution over a neuron's firing probability, which in general is skewed and non-Gaussian (Figure 3A upper right). From this function we compute (Methods) both the neuron's mean firing probability and the pairwise correlation of two identical neurons following this profile (Figure 3A lower right). Example samples from the model are illustrated in Figure 3B.

Neural firing rates and correlations had qualitatively different dependencies on the underlying logistic model's slope and threshold. Neural firing rate was greatest when threshold was low and slope was high (top left of phase plot, Figure 3C left), whereas correlations were greatest

when both threshold and slope were high (top right of phase plot, Figure 3C right). This implies that any change in the circuit's input-output function slope or threshold will in general have distinct effects on firing rate versus correlations, and so could not be captured by a 1-dimensional E/I balance model that sought to normalize firing rates alone. To illustrate this fact, we plot the calculated correlation values along a contour where firing probability is fixed at 0.1

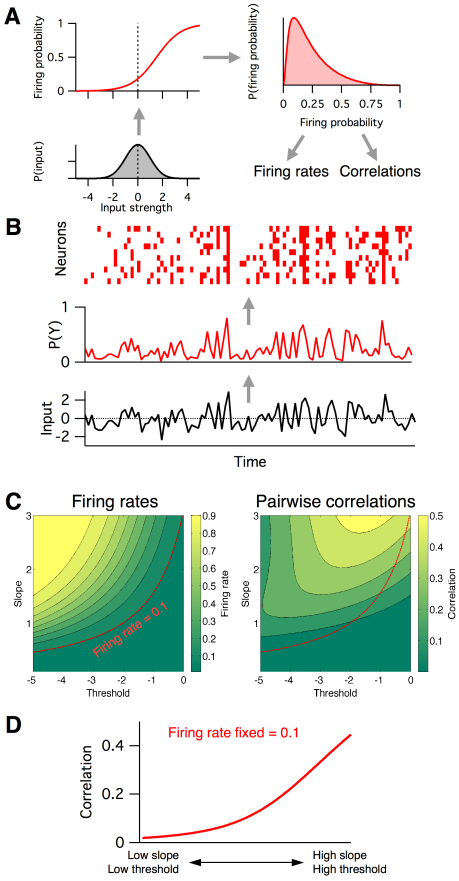

Figure 3. Firing rates and pairwise correlations from the logistic response model.
A: Logistic model components. We assume a normally distributed input drive (gray distribution, bottom left), which is passed through the neuron's probabilistic spike input-output function (red curve, top left), which results in a distribution of spike probabilities (top right) that are determined by the input-output function's slope and threshold parameters. From the output distribution we can directly calculate the mean firing rate and correlation between a pair of such neurons (Methods).
B: Example spikes from the logistic model. The bottom trace (black) shows examples inputs over time drawn randomly from the same normal distribution. This is transformed to spike probability at each time point (red trace). Example spike trains can then be generated from the spike probability trace by drawing Bernoulli samples with the specified probabilities (red ticks, top). If each neuron's spike train is conditionally independent given the same spike probabilities, we can see correlations in their spike trains.

C: Calculated mean firing rate (left) and pairwise correlation (right) color maps as a function of the logistic threshold (x-axis) and slope (y-axis) parameters. Contours indicate lines of fixed firing rate or correlation in the 2D slope-threshold space.
D: Pairwise correlation values along the slope-threshold contour for firing rate = 0.1.

(Figure 3D). In the region of parameter space where both the slope and threshold are low (Figure 3C bottom left), correlations are low, ~0.01. However, as we move along the contour for firing rate = 0.1 towards the region of parameter space where slope and threshold are high (Figure 3C top right), the pairwise correlations increase to ~0.4. This shows that a 1-dimensional E/I balance rule that exclusively sought to normalize neural firing rates would leave neural correlations free to achieve arbitrary values.

How might these findings inform our understanding of neurodevelopmental disorders, such as Fragile-X syndrome? To explore this we fit the parameters of the logistic model to reproduce the statistics of spontaneous activity recorded from populations of neurons in unanesthetized mouse somatosensory cortex using in vivo two-photon Ca^{2+} imaging (data previously published in (Gonçalves et al., 2013), see Methods for experimental details). We compared the data from wild-type (WT) mice with *Frm1* KO mice, the best studied animal model for Fragile-X syndrome, across three different developmental time points: just before (P9—11) and after (P14—16) the critical period, and a more mature timepoint (P30—40). Example ΔF/F raster plots from each group are shown in Figure 4A. We binned the data into 1 s timebins (originally imaged at 4 Hz), then transformed each neuron's timeseries of ΔF/F values into a probabilistic sequence of binary ON/OFF values by assuming a Poisson firing model (Methods). We then summarized the neural population activity from each animal with three statistics: the mean ON probability across all recorded neurons (Figure 4C), the standard deviation (s.d.) in ON probability across neurons (Figure 4D), and the mean correlation between all pairs of neurons (Figure 4E). Together these measures capture both the statistics of the bulk population activity and some indication of the heterogeneity across neurons. Samples from the fitted models for each experimental group are shown in Figure 4B. For mean firing rates, the only change we detected was a decrease in firing probability in WT between P14—16 and P30—40 ($p = 0.027$), which was coupled with an increased s.d. of firing rates ($p = 0.015$). We also detected a higher firing rate s.d. in P9—11 KO animals than WT ($p = 0.031$). Finally, as previously reported (Golshani et al., 2009; Gonçalves et al., 2013; Rochefort et al., 2009), we found a substantial

decrease in pairwise correlations in both genotypes across development, with slightly higher correlations in KO animals than WT at P9—11 ($p = 0.029$) and P14—16 ($p = 0.047$). These results are consistent with a general model where neural firing becomes desynchronized and sparsified around the critical period, at least in WT animals (Golshani et al., 2009; Rochefort et al., 2009).

For the three summary statistics from each animal, we used a gradient descent algorithm to find the five parameters of a population-level version of the logistic model that best matched the activity statistics (see Methods). For each animal, we plot the mean slope and mean threshold fits (Figure 4F) on top of the previously calculated (Figure 3C) 2D slope-threshold maps of firing rate and correlation. We find that in young animals, P9—11, most points are scattered at high values of both slope and threshold (Figure 4D left). With age, the parameter fits for both genotypes moved south-west towards the low slope and low threshold region of parameter space (Figure 4D center and right). The mean location of the cloud of points at each developmental age differed between WT and KO. We plot the direction of shift in group mean from WT to KO in Figure 4G. In young animals, P9—11 and P14—16, the KO group had both higher slope and higher threshold than WT, whereas in adult animals, P30—40, the KO group had a lower slope and lower threshold than WT. These results demonstrate an opposite direction of circuit parameter change in young Fragile-X mice compared to adults, which could not be captured by examining either neural firing rates or correlations.

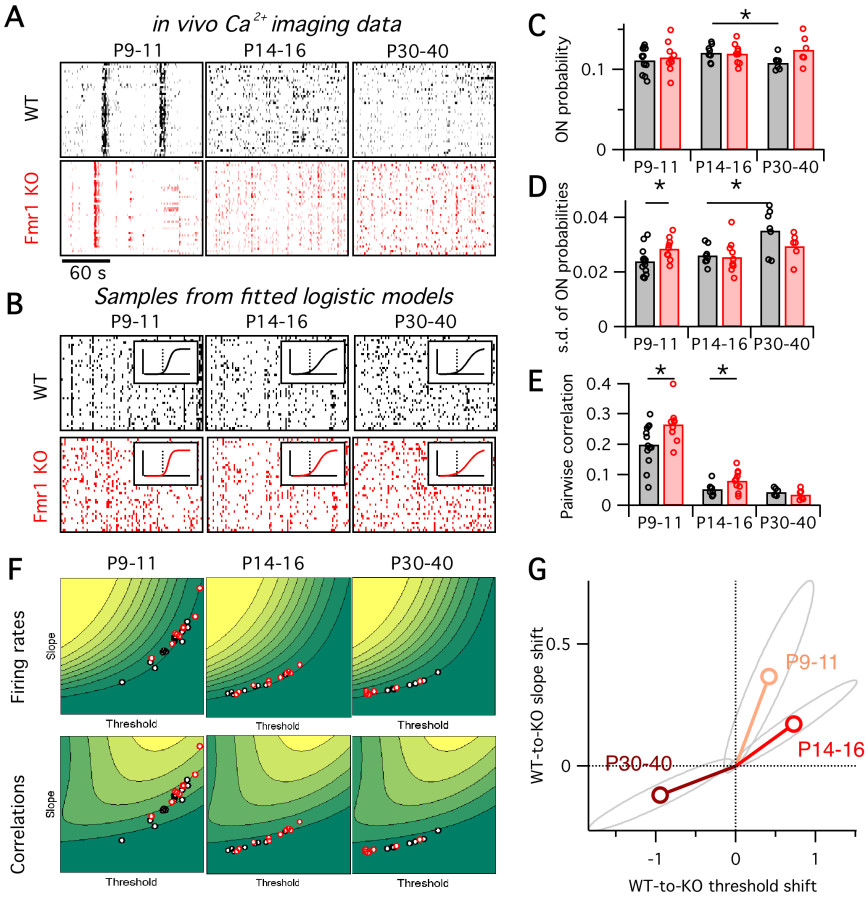

Figure 4. Fragile-X fits from logistic model.
A: Example Ca^{2+} imaging dF/F raster plots from a single animal from each of two genotypes, WT and *Frm1* KO, and three age groups, P9—11, P14—16 and P30—40. In each case 3 minutes of data are shown from 40 neurons.
B: Example samples from the fitted logistic models, corresponding to the six groups shown in panel A. Inset shows group mean fitted logistic function, dashed vertical line represents zero.
C-E: Mean firing probability (C), standard deviation of firing probabilities (D) and mean pairwise correlation across all neurons (E). Each circle represents data from a single animal, bars represent group means.
F: Fitted logistic mean slope and mean threshold values for data from each WT (black circles) and *Fmr1* KO (red circles) animal. Values overlaid on same firing rate (top) and correlation (bottom) maps from Figure 3C.
G: Shift in mean logistic slope and threshold values from WT to KO for P9—11 (orange), P14—16 (red) and P30—40 (brown). Grey ellipses represent 95% confidence intervals (Methods).

Earlier we asked how sensitive the logistic model slope and threshold parameters were to alterations in the many underlying neural circuit components (Figure 2). In a similar way, we

can also ask how sensitive the neural firing rates and correlations are to alterations in the logistic slope and threshold parameters. This is important since inspection of the 2-dimensional maps in Figure 2C shows that these sensitivities will differ depending on starting location within the slope-threshold space. To quantify this effect, we calculated the sensitivity of both the firing rate and correlations to small changes in the slope and threshold (Figure 5, see Methods), local to the fitted logistic parameter values for each animal (black and red circles in Figure 4F). Across all animals, we found that changes in the slope and threshold were qualitatively consistent but quantitatively inconsistent. Increasing the slope or decreasing the threshold always increased both firing rates and correlations. However, the magnitude of these effects depended strongly on developmental age (we found only minor differences between genotypes at any age). In young animals, P9—11, changes in the logistic threshold (solid bars in Figure 5) had substantial effects on both firing rates and correlation. This sensitivity decreased with age ($p \leq 0.013$ for firing rates, $p < 0.01$ for correlations from P9—11 to P14—16, both for pooled data across genotypes), so that in adult animals, P30-40, changes in threshold had relatively little effect on neural activity statistics. A different picture emerged for the logistic slope parameter (striped bars in Figure 5). There, the firing rate sensitivity increased with from P9—11 to P14—16 ($p < 1e\text{-}6$) (Figure 5A), while correlation sensitivity stayed approximately constant ($p \geq 0.18$) (Figure 5B). These results show that the quantitative relationships between neural activity statistics and the underlying circuit parameters are not fixed across development.

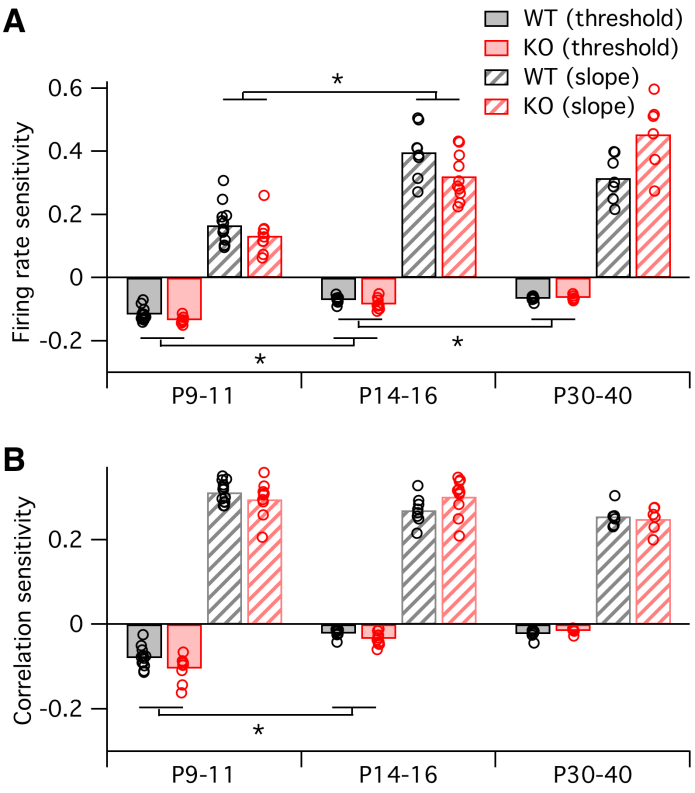

Figure 5. Sensitivity of firing rate and correlations with respect to logistic model parameters, local to the parameter fit for each animal.
Sensitivity of firing probability (**A**) and pairwise correlations (**B**) to change in threshold (solid bars) and slope (striped bars) parameters of logistic model, about the fitted parameter values for each animal (circles) displayed in Figure 4F. Bars represent group means. Each statistical test compares the mean values between adjacent pairs of age groups, where the data were pooled between genotypes.

What are the functional implications of these alterations in firing rates and correlations in Fragile-X mice across development? To address this, we attempted to calculate the entropy of the neural population activity for the data from each animal. Entropy is a quantity from information theory, measured in bits, that puts a hard upper bound on the amount of information that can be represented by any coding system (Cover and Thomas, 2006). Intuitively, the entropy measures how uniform the neural population activity pattern distribution is: it is large if the circuit exhibits many different activity patterns over time, and small if only a few activity patterns dominate. Entropy is an appealing measure for the present problem because it is sensitive both to neural firing rates and to correlations at all orders. It is typically

highest when firing rates are high and correlations are low. Although entropy is notoriously difficult to calculate for large neural populations because most estimation methods require impractically long data recordings (Quian Quiroga and Panzeri, 2009), we recently developed a new statistical method for this purpose, called the *population tracking model*, that scales well to large numbers of neurons, even for limited data (O'Donnell et al., 2017). We fit this population tracking model to the same Ca^{2+} imaging data as analyzed above (Figure 6). An intermediate step in estimating the neural entropy involves calculating a low-parameter approximation of the entire probability distribution over all 2^N neural population activity patterns, where N is the number of neurons. The cumulatives of these probability distributions calculated for 50-neuron subsets of the recordings are shown in Figure 6A. In young animals P9—11, a small number of activity patterns accounts for a large fraction of the probability mass (Figure 6A left). For example, based on these curves, 50% of the time we would expect to see the same 1000—10,000 patterns out of a possible total $2^{50} \approx 10^{15}$ patterns. In contrast, in older animals P14—16 and P30—40 the cumulative distributions shift rightwards so that more patterns are typically observed (Figure 6A center, right). In these cases, around 1,000,000 patterns are needed to account for 50% probability mass.

Instead of attempting to quantify these shifts by asking how many patterns are needed to cross an arbitrary threshold of probability mass, we instead calculated the entropy, which takes into account the shape of the entire probability distribution. The entropy depends on the number of neurons analyzed, so we normalized all estimates to calculate the entropy per neuron (Figure 6B—C). Since we are treating neurons as binary, the entropy/neuron was bounded between 0 and 1 bits. For all age groups, and for both WT and *Fmr1* KO animals, entropy/neuron progressively decreased with the number of neurons analyzed (Figure 6B). Because each imaging session captured a different number of neurons (range 40—198, median 97), we fit the entropy/neuron versus number of neurons data with a double exponential function (see Methods) and use the fit to provide a standardized estimate of the entropy/neuron for 100-neuron populations (Figure 6C). In WT animals, entropy/neuron showed a non-monotonic trajectory across development (O'Donnell et al., 2017). At P9—11 it was low, 0.38 bits (95% c.i. [0.35:0.41]), before increasing at P14—16 ($p < 0.001$) to 0.50 bits (95% c.i. [0.48:0.52]), before

297 decreasing again at P30—40 (p = 0.028) to 0.45 bits (95% c.i. [0.42:0.48]). We found a
298 different entropy trajectory in *Frm1* KO animals. There, although entropy/neuron also began
299 low at 0.34 bits (95% c.i. [0.30:0.39]), not different from WT (p= 0.19), when it increased at
300 P14—16 (p < 0.001) to 0.465 bits (95% c.i. [0.45:0.48]) it remained lower than for WT (p =
301 0.048). Finally, instead of decreasing as in the WT case, entropy continued to increase in
302 P30—40 *Fmr1* KO animals (p = 0.033) to 0.51 bits (95% c.i. [0.47:0.55]), higher than WT (p =
303 0.034). These entropy values estimated directly from Ca^{2+} imaging data agreed well with
304 entropy estimates for synthetic data sampled from the previously fit logistic models
305 (Supplementary Figure 1). In summary, unlike WT animals, *Fmr1* KO mice showed a
306 monotonically increasing entropy/neuron from P9—11 to P30—40. Furthermore, the direction
307 of change in entropy between P14—16 and P30—40 was opposite for WT and *Fmr1* KO
308 animals, decreasing in the former and increasing in the latter.

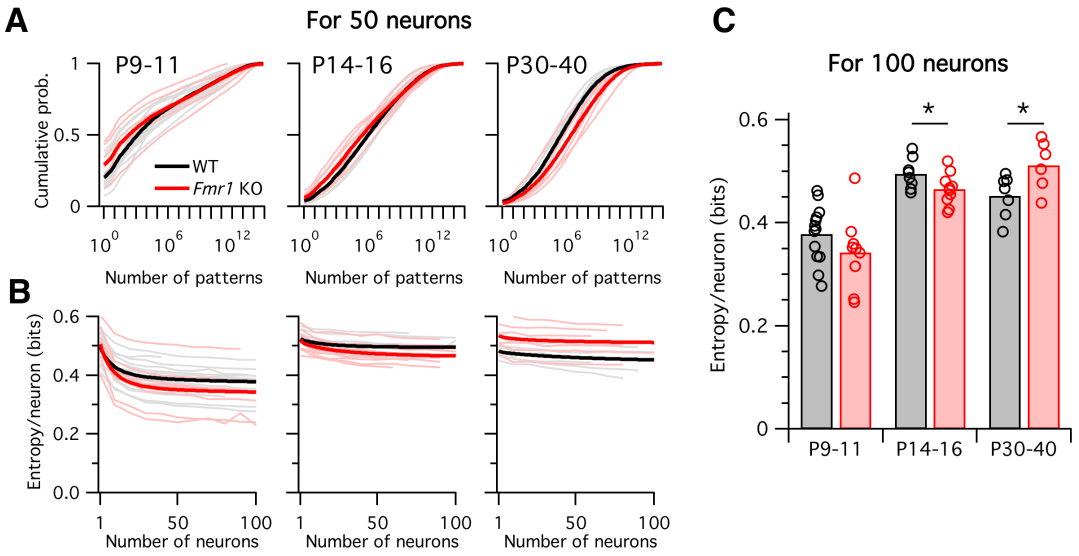

Figure 6. Differing trajectories of WT and KO entropy across development.
A: Cumulative probability mass as a function of the number of patterns. Patterns ordered from most probable to least probable. Thin lines are mean across many randomly-chosen 50-neuron subsets from a given animal, and thick lines represent means across all animals of a given genotype.
B: Entropy per neuron as a function of the number of neurons analyzed. Thin lines are mean across many randomly chosen subsets for a given animal, thick lines are group mean of double exponential fits to the data (see Methods). Age groups (left to right) are as in panel A.
C: Estimated entropy/neuron for 100 neuron populations. Circles represent individual animals, bars are group means.

Discussion

The 1-dimensional E/I imbalance model has been widely used for interpreting neural circuit changes observed in animal models of diverse brain disorders (Bateup et al., 2011; Dani et al., 2005; Gibson et al., 2008; Kehrer et al., 2008; Wallace et al., 2012). In the case of Fragile-X syndrome, the hyperexcitability prediction of the E/I imbalance model is consistent with many of the symptoms of the disease (e.g. seizures, hyperarousal, hyperactivity, hypersensitivity to sensory stimuli) and the known pathogenic defects implicated in *Fmr1* KO mice (diminished GABA signaling, exaggerated intrinsic excitability, increased neuronal firing rates; reviewed by (Contractor et al., 2015)). Here we extended this thinking to test the hypothesis that the E/I imbalance model can account for alterations in other neural activity statistics beyond the mean firing rates. However, our results demonstrate that it cannot. The model was too inflexible to account for the joint alterations in both neural firing rates and correlations observed in Fragile-X model mice. This suggests that future studies of brain disorders may need to consider higher-dimensional models of neural circuit dysfunction.

First, we built a detailed computational model of a specific neural circuit, L2/3 of mouse somatosensory cortex (Figure 1), and asked how sensitive the spiking responses of the overall circuit were to changes in its underlying neural components, many of which are known to be altered in *Fmr1* KO mice (Bureau et al., 2008; Gibson et al., 2008; Gonçalves et al., 2013; Harlow et al., 2010; Hays et al., 2011; Paluszkiewicz et al., 2011; Patel et al., 2013; Testa-Silva et al., 2012). We found that while changing some neural parameters did have a large effect, changing of other parameters had little or no effect on circuit function (Figure 2B). This property, termed sloppiness, has been reported as widely prevalent in computational models of biological systems (Gutenkunst et al., 2007; O'Leary et al., 2015). Its existence has two important implications for studies of brain disorders: first, many of the physiological component changes discovered in animal models may be entirely benign at the circuit level. Second, any treatment designed to correct circuit function does not necessarily need to correct all of the low-level properties in order to be successful.

In addition to the varying magnitudes of circuit components' effect on circuit function, we also found that different components shifted the circuit input-output function in different directions, as defined by our 2D logistic response model (Figures 1 and 2). Even circuit parameters that are nominally of the same type, such as the strength of glutamatergic synapses between excitatory (E) neurons in L4 to E neurons in L2/3 or synaptic strength between E neurons within L2/3, had qualitatively different effects on the circuit response to stimulation (Figure 2). According to the standard E/I imbalance model (Rubenstein and Merzenich, 2003), both of these parameters should have similar effects on circuit function; but according to the logistic response model we studied, their differing effects on slope and threshold parameters must necessarily lead to different magnitudes of change in neural firing rates and correlations (Figure 3C). Indeed, no 1-dimensional model of circuit function could ever capture the heterogeneity in parameter sensitivities that we observed (Figure 2B).

Next, we fit the parameters of the logistic response model to match the *in vivo* firing statistics of neural populations from WT and *Fmr1* KO mice of varying age (Figure 4). Previous studies had found that neural correlations decrease during development (Golshani et al., 2009; Rochefort et al., 2009), and that early postnatal *Fmr1* KO mice had higher correlations and firing rates than WT mice (Gonçalves et al., 2013; La Fata et al., 2014). A recent study suggests circuit hypersynchrony is also found in different mouse models of Rett syndrome (Lu et al., 2016). However, the relationship between these changes in firing statistics and the underlying neural circuit components were unclear. Our logistic model helps bridge this gap, leading to two findings: first, the direction of circuit parameter change from young (P9—11 and P14—16) to mature (P30—40) animals is opposite in WT to KO mice (Figure 4G). Similar opposing switches in sensory cortex properties with age were also recently reported in *Frm1* KO rats (Berzhanskaya et al., 2016). Second, we found that the sensitivity of neural firing rates and correlations to changes in underlying circuit components depends on developmental age (Figure 5). Taken together, these findings imply that qualitatively different interventions may be needed at different stages of development in Fragile-X, and perhaps other neurodevelopmental disorders, to shift cortical circuit function towards typical wild-type operation.

Spontaneous, intrinsic activity is ubiquitously present in mammalian cerebral cortex. It is highly structured at multiple spatiotemporal scales (Mitra et al., 2015; Ringach, 2009) and interacts strongly with the signals evoked by sensory stimulation (Ringach, 2009). Cellular-resolution recordings in animals have shown that the patterns of spontaneous activity in neural populations are representative of the ensemble of activity patterns used by the brain to represent sensory stimuli (Berkes et al., 2011; Luczak et al., 2009; Miller et al., 2014). Here we found that the entropy of spontaneous activity in WT mouse somatosensory cortex follows an inverted-U shaped trajectory across development, and that this trajectory is dramatically altered in the *Fmr1* KO mouse model of Fragile-X (Figure 6). Although we saw no reliable differences across genotypes in early postnatal animals (P9—11), *Fmr1* KO animals showed lower entropy than WT after the second postnatal week (P14—16), while surprisingly switching to show higher entropy than WT in adult (P30—40). Notably, this switch in the direction of entropy change from WT to KO during development mirrors the reversing we saw in logistic model parameter changes in Figure 4G. Together, these findings suggest a perturbed trajectory of cortical development during the critical period in *Fmr1* KO mice (Meredith et al., 2012). However, our results cannot distinguish whether the observed perturbation in L2/3 activity statistics reflects a developmental delay, or a permanently altered developmental trajectory. Further studies at later developmental time points are needed.

What is the functional significance of these shifts in population entropy? Previous work suggested that the entropy of neural circuit activity may be optimally tuned at intermediate levels as a trade-off between maximizing representational capacity at high entropy, versus maintaining error correction and regularization at low entropy (Schneidman et al., 2006). These properties can also be thought of as trading off between discrimination and generalization, respectively (Qian and Lipkin, 2011). If we assume that WT mice are optimally tuned, our findings predict that young *Fmr1* KO mice should show poorer somatosensory discrimination in behavioral tasks than wild-type animals, while in contrast adult *Fmr1* KO mice should perform more poorly on tasks involving generalization across somatosensory stimuli.

If the 1-dimensional E/I imbalance model is not sufficiently rich to capture the circuit changes observed in neurodevelopmental disorders, what should it be replaced with? How many

dimensions or degrees of freedom should a working model for a brain disorder have? We suggest that the most promising approach is to start by considering the computational function of a particular neural circuit, then working backwards to design a model that is both sophisticated enough to capture the key information processing features of the circuit, but simple enough to interpret and link to physiological data. In this study we considered a 2-parameter model of L2/3 somatosensory cortex's input-output function, which could account for both neural firing rates and correlations. Other brain circuits may demand models with more degrees of freedom. Crucially, the most informative models need not be those that include the highest level of physiological detail. All models are ultimately wrong in the sense that they make abstractions about their underlying parts, and detailed models carry the additional burden of fitting many parameters, which may be difficult to adequately constrain (O'Leary et al., 2015).

One potential use of simple parametric circuit models such as the ones we employed here may be as a tool for rationally designing candidate intervention compounds and then screening their effects on neural population activity. For example, the current study could have been extended to fit the logistic model to neural activity data from another cohort of *Frm1* KO mice that had received a candidate treatment, then ask if the fitted model parameters were closer in value to those from WT animals or *Fmr1* KO controls. Approaches like this could complement the traditional strategy of designing drugs based on reversing molecular deficits and then assessing the drug's impact on animal model behavior. Indeed, our results suggest that given the multi-dimensionality of circuit properties, it may prove difficult or impossible to find a single compound that can correctly reverse deficits at any age. This scenario might require a combination of drugs chosen to push circuit-level properties towards the 'correct' region of parameter space. The framework we have introduced in this study can facilitate this type of high-dimensional intervention analysis for diverse neurodevelopmental disorders.

Materials and Methods

Mouse in vivo calcium imaging recording

All Ca^{2+} imaging data were published previously (Gonçalves et al., 2013). Briefly, data were collected from male and female C57Bl/6 wild-type mice at P9–40. Mice were anesthetized with isoflurane, and a cranial window was fitted over primary somatosensory cortex by stereotaxic coordinates. Mice were then transferred to a two-photon microscope and headfixed to the stage while still under isoflurane anesthesia. 2—4 injections of the Ca^{2+} sensitive Oregon-Green BAPTA-1 (OGB) dye and sulforhodamine-101 (to visualize astrocytes) were injected 200 um below the dura. Calcium imaging was performed using a Ti-Sapphire Chameleon Ultra II laser (Coherent) tuned to 800 nm. Imaging in unanesthetized mice began within 30-60 mins of stopping the flow of isoflurane after the last OGB injection. Images were acquired using ScanImage software (Pologruto et al., 2004) written in MATLAB (MathWorks). Whole-field images were collected using a 20× 0.95 NA objective (Olympus) at an acquisition speed of 3.9 Hz (512 × 128 pixels). Several 3-minute movies were concatenated and brief segments of motion artifacts were removed (always <10 s total). Data were corrected for x—y drift. Cell contours were automatically detected and the average ΔF/F signal of each cell body was calculated at each time point. Each ΔF/F trace was low-pass filtered using a Butterworth filter (coefficient of 0.16) and deconvolved with a 2 s single-exponential kernel (Yaksi and Friedrich, 2006). To remove baseline noise, the standard deviation of all points below zero in each deconvolved trace was calculated, multiplied by two, and set as the positive threshold level below which all points in the deconvolved trace were set to zero. Estimated firing rates of the neurons, $r_i(t)$, were then obtained by multiplying the deconvolved trace by a factor previously derived empirically from cell-attached recordings in vivo (Golshani et al., 2009).

Computational methods

Data analysis and logistic model calculations were done using MATLAB (Mathworks).

Detailed layer 2/3 model simulations

Layer 2/3 model simulations (Figures 1 and 2) were implemented with the Python-based simulator Brian (http://briansimulator.org/) (Goodman and Brette, 2009), and results analyzed with MATLAB (Mathworks). The model consisted of four populations of reciprocally connected

leaky integrate-and-fire neurons representing a L2/3 somatosensory barrel circuit: 1700 excitatory neurons, 70 PV inhibitory neurons, 115 $5HT_{3A}R$ inhibitory neurons, and 45 SOM inhibitory neurons, driven by a separate population of 1500 excitatory spike sources representing input from L4. Cell numbers were estimated by combining layer-specific excitatory and inhibitory cell count information from (Lefort et al., 2009) with the approximate percentages of the three inhibitory cell groups given by (Petersen and Crochet, 2013). All synaptic connections were formed probabilistically by drawing independent random Bernoulli variables with connection type-specific probabilities. Synaptic PSP amplitudes were drawn independently for each synapse from a log-normal distribution constrained by the experimentally reported mean and median values for each particular connection type. Synapses in the model were conductance-based, but since synaptic strengths reported in the literature were typically in terms of EPSP/IPSP amplitude, in accordance with how the experiments were performed (Avermann et al., 2012), we set each maximal synaptic conductance as the value needed to generate a PSP of the desired amplitude when the target neuron started at resting potential in the case of EPSPs or -55mV in the case of IPSPs, which we computed analytically. Refractory periods were calculated as the inter-spike-interval corresponding to the maximal experimentally reported firing rate. Release probability and synaptic strength values for unconnected neurons are excluded from Table 1. Excitatory synaptic time constants were set at 2 ms, which is typical for the fast component of AMPA receptor responses, but could not be estimated from the PSP statistics in (Avermann et al., 2012) because of masking by the slower membrane time constant. The mathematical form of our model meant that inhibitory synaptic time constants needed to be equal for all incoming inhibitory synapses to a neuron. We set these to 40 ms for E, $5HT_{3A}R$ and SOM neurons and 16 ms for PV neurons, which were the typical values of the IPSP decay time constants in the (Avermann et al., 2012) dataset. Due to lack of direct data for this circuit, connection probabilities for synapses from L4 E neurons to E, PV and SOM L2/3 neurons was set to a typical cortical value of 0.15, while $5HT_{3A}R$ neurons did not receive any input from L4 (Gentet et al., 2012). Similarly due to a lack of direct data, we set synaptic release probabilities for connections from L4 to L2/3 neurons to a typical cortical value of 0.25, while mean and median L4 excitatory PSP amplitudes onto L2/3 PV and SOM were set to 0.8 and 0.48 mV,

481 respectively, to match reported data for L4 EPSP amplitudes onto L2/3 E neurons (Lefort et al.,
482 2009). L4 neuron dynamics were not explicitly simulated, but instead modeled only as a set of
483 output spike trains. After selecting the subset of active L4 neurons (see Results), spike times
484 were drawn randomly from a Gaussian distribution with standard deviation of 2 ms.

485 For the simulations presented in Figure 2 we varied only 76 model parameters, which is 24
486 less than the total number of 100 model parameters listed in Table 1. We excluded the four
487 neuronal refractory periods (because in almost all simulations each neuron spiked a maximum
488 of once, making the refractory period irrelevant), and the six connection probabilities that were
489 fixed at zero. Finally, we grouped together the mean and median PSP amplitudes for each of
490 the fourteen non-zero synaptic connections, so that both parameters were increased or
491 decreased by the same fraction in tandem. Together these choices reduced the number of test
492 parameters from 100 to 76.

493 For all parameters that naturally range from 0 upwards, such as the number of neurons or
494 release probability, we increased or decreased their values during testing in the most intuitive
495 way, by adding +/- 20% of the baseline value. However, this method was less useful for other
496 parameters, such as cell resting voltage, for which we reasoned it made more sense to scale
497 relative to another parameter, such as spike threshold. As a result, we varied 1) resting voltage
498 relative to its difference from spike threshold; 2) spike threshold relative to its difference with
499 resting voltage; 3) excitatory synaptic reversal potentials relative to resting voltage; 4) inhibitory
500 synaptic reversal potentials relative to spike threshold.

Table 1. L2/3 computational circuit model parameters and mean slope & threshold shifts.

Parameter	Value	Source	+20% effect on slope, thresh	Parameter	Value	Source	+20% effect on slope, thresh
N_E	1700	[1]	slope: 6.4 x10^{-3} thresh: 5.16	$pcon_{I5htE}$	0.465	[2]	slope: -3.25 x10^{-3} thresh: -0.103
N_{Ipv}	70	[1]	slope: 4.3 x10^{-3} thresh: -1.51	$pcon_{I5htIpv}$	0.38	[2]	slope: -7.13 x10^{-3} thresh: -0.298
N_{I5ht}	115	[1]	slope: -0.0104 thresh: -0.58	$pcon_{I5htI5ht}$	0.38	[2]	slope: 6.07 x10^{-4} thresh: 0.175
N_{Isom}	45	[1]	slope: -0.001 thresh: -0.83	$pcon_{I5htIsom}$	0	No data	Not tested
N_{EL4}	1500	[1]	slope: -0.106 thresh: 3.43	$pcon_{IsomE}$	0.5	[5]	slope: -6.29 x10^{-3} thresh: -0.8919
$Vrest_E$	-68 mV	[2]	slope: 0.049 thresh: -6.09	$pcon_{IsomIpv}$	0	No data	Not tested
$Vrest_{Ipv}$	-68 mV	[2]	slope: -0.016	$pcon_{IsomI5ht}$	0	No data	Not tested

			thresh: -0.963				
$Vrest_{l5ht}$	-62 mV	[2]	slope: -9.48 x10^{-4} thresh: 0.205	$pcon_{lsomlsom}$	0	No data	Not tested
$Vrest_{lsom}$	-57 mV	[3]	slope: 3.58 x10^{-3} thresh: 0.034	$prel_{EL4E}$	0.25	No data	slope: -0.112 thresh: 4.21
Vth_{E}	-38 mV	[2]	slope: -3.76 x10^{-3} thresh: -0.381	$prel_{EL4lpv}$	0.25	No data	slope: 0.0103 thresh: 0.682
Vth_{lpv}	-37.4 mV	[2]	slope: 3.87 x10^{-3} thresh: 0.221	$prel_{EL4lsom}$	0.25	No data	slope: -2.06 x10^{-3} thresh: -0.537
Vth_{l5ht}	-36 mV	[2]	slope: -1.12 x10^{-3} thresh: 0.013	$prel_{EE}$	0.25	No data	slope: 4.99 x10^{-3} thresh: 6.074
Vth_{lsom}	-40 mV	[3]	slope: -3.26 x10^{-3} thresh: -0.083	$prel_{Elpv}$	0.25	No data	slope: -4.04 x10^{-4} thresh: 0.163
Rin_{E}	160 MΩ	[2]	slope: 1.95 x10^{-3} thresh: -0.283	$prel_{El5ht}$	0.25	No data	slope: -9.32 x10^{-3} thresh: -0.532
Rin_{lpv}	100 MΩ	[2]	slope: -8.38 x10^{-3} thresh: -0.283	$prel_{Elsom}$	0.25	No data	slope: -7.32 x10^{-3} thresh: -0.3847
Rin_{l5ht}	200 MΩ	[2]	slope: -3.87 x10^{-3} thresh: -0.653	$prel_{lpvE}$	0.25	No data	slope: 1.03 x10^{-2} thresh: -0.941
Rin_{lsom}	250 MΩ	[4]	slope: 7.55 x10^{-3} thresh: 0.465	$prel_{lpvlpv}$	0.25	No data	slope: 1.21 x10^{-3} thresh: -0.061
τm_{E}	28 ms	[2]	slope: -9.59 x10^{-3} thresh: 0.268	$prel_{lpvl5ht}$	0.25	No data	slope: -4.73 x10^{-3} thresh: 0.011
τm_{lpv}	21 ms	[2]	slope: 4.82 x10^{-3} thresh: 0.027	$prel_{l5htE}$	0.25	No data	slope: -1.63 x10^{-3} thresh: -0.379
τm_{l5ht}	10 ms	[2]	slope: -5.09 x10^{-3} thresh: -0.302	$prel_{l5htlpv}$	0.25	No data	slope: -3.41 x10^{-3} thresh: -0.262
τm_{lsom}	30 ms	[4]	slope: -2.89 x10^{-3} thresh: -0.159	$prel_{l5htl5ht}$	0.25	No data	slope: 3.05 x10^{-3} thresh: 0.123
$tref_{E}$	55.5 ms	[2]	Not tested	$p_{rel,lsomE}$	0.25	No data	slope: -2.13 x10^{-4} thresh: -0.65
$tref_{lpv}$	5.4 ms	[2]	Not tested	$w_{EL4E,mean}$	0.8 mV	[1]	slope: -0.142 thresh: 0.342
$tref_{l5ht}$	21.3 ms	[2]	Not tested	$w_{EL4E,median}$	0.48 mV	[1]	slope: -0.142 thresh: 0.342
$tref_{lsom}$	20 ms	[3]	Not tested	$w_{EL4lpv,mean}$	0.8 mV	$=w_{EL4E}$	slope: 3.61 x10^{-3} thresh: 6.54 x10^{-3}
$\tau syn_{E,e}$	2 ms	Typical	slope: 1.37 x10^{-2} thresh: -1.79	$w_{EL4lpv,median}$	0.48 mV	$=w_{EL4E}$	slope: 3.61 x10^{-3} thresh: 6.54 x10^{-3}
$\tau syn_{E,i}$	40 ms	[2]	slope: -7.29 x10^{-3} thresh: 0.48	$w_{EL4lsom,mean}$	0.8 mV	$=w_{EL4E}$	slope: 5.05 x10^{-3} thresh: -0.329
$\tau syn_{lpv,e}$	2 ms	Typical	slope: -9.79 x10^{-3} thresh: -0.477	$w_{EL4lsom,median}$	0.48 mV	$=w_{EL4E}$	slope: 5.05 x10^{-3} thresh: -0.329
$\tau syn_{lpv,i}$	16 ms	[2]	slope: 1.56 x10^{-3} thresh: -0.097	$w_{EE,mean}$	0.37 mV	[2]	slope: 7.44 x10^{-3} thresh: 5.34
$\tau syn_{l5ht,e}$	2 ms	Typical	slope: 4.52 x10^{-3} thresh: -0.047	$w_{EE,median}$	0.2 mV	[2]	slope: 7.44 x10^{-3} thresh: 5.34
$\tau syn_{l5ht,i}$	40 ms	[2]	slope: -3.82 x10^{-3} thresh: -0.387	$w_{Elpv,mean}$	0.82 mV	[2]	slope: -3.77 x10^{-4} thresh: -0.297
$\tau syn_{lsom,e}$	2 ms	Typical	slope: -0.0126 thresh: -8.82 x10^{-3}	$w_{Elpv,median}$	0.68 mV	[2]	slope: -3.77 x10^{-4} thresh: -0.297
$\tau syn_{lsom,i}$	40 ms	[2]	slope: -4.88 x10^{-3} thresh: -0.301	$w_{El5ht,mean}$	0.39 mV	[2]	slope: -6.81 x10^{-3} thresh: -0.46
$Erev_{e}$	0 mV	Typical	slope: -0.056 thresh: 1.53	$w_{El5ht,median}$	0.19 mV	[2]	slope: -6.81 x10^{-3} thresh: -0.46
$Erev_{Ei}$	-68 mV	$=Vrest_{E}$	slope: 3.2x10^{-3} thresh: -3.77	$w_{Elsom,mean}$	0.5 mV	No data	slope: -3.61 x10^{-3} thresh: -0.359
$Erev_{lpvi}$	-68 mV	$=Vrest_{lpv}$	slope: -0.010	$w_{Elsom,median}$	0.4 mV	No data	slope: -3.61 x10^{-3}

			thresh: -0.617				thresh: -0.359
$Erev_{I5hti}$	-62 mV	$=Vrest_{I5ht}$	slope: $3.8x10^{-3}$ thresh: 0.132	$w_{IpvE,mean}$	0.52 mV	[2]	slope: 6.41 $x10^{-3}$ thresh: -1.47
$Erev_{Isomi}$	-57 mV	$=Vrest_{Isom}$	slope: $-4.2x10^{-3}$ thresh: -0.088	$w_{IpvE,median}$	-0.29 mV	[2]	slope: 6.41 $x10^{-3}$ thresh: -1.47
$pcon_{EL4E}$	0.15	No data	slope: -0.121 thresh: 2.99	$w_{IpvIpv,mean}$	-0.56 mV	[2]	slope: -2.52 $x10^{-3}$ thresh: -0.345
$pcon_{EL4Ipv}$	0.15	No data	slope: $1.38x10^{-3}$ thresh: 0.029	$w_{IpvIpv,median}$	-0.44 mV	[2]	slope: -2.52 $x10^{-3}$ thresh: -0.345
$pcon_{EL4I5ht}$	0	No data	Not tested	$w_{IpvI5ht,mean}$	-0.83 mV	[2]	slope: -4.24 $x10^{-3}$ thresh: -0.266
$pcon_{EL4Isom}$	0.15	No data	slope: 7.62 $x10^{-3}$ thresh: -0.245	$w_{IpvI5ht,median}$	-0.6 mV	[2]	slope: -4.24 $x10^{-3}$ thresh: -0.266
$pcon_{EE}$	0.17	[2]	slope: 5.86 $x10^{-3}$ thresh: 6.084	$w_{I5htE,mean}$	-0.49 mV	[2]	slope: -3.61 $x10^{-4}$ thresh: -0.018
$pcon_{EIpv}$	0.575	[2]	slope: -1.17 $x10^{-3}$ thresh: -0.099	$w_{I5htE,median}$	-0.3 mV	[2]	slope: -3.61 $x10^{-4}$ thresh: -0.018
$pcon_{EI5ht}$	0.24	[2]	slope: -6.44 $x10^{-3}$ thresh: -0.541	$w_{I5htIpv,mean}$	-0.49 mV	[2]	slope: -1.77 $x10^{-3}$ thresh: -0.187
$pcon_{EIsom}$	0.5	[5]	slope: -4.37 $x10^{-3}$ thresh: -0.27	$w_{I5htIpv,median}$	-0.15 mV	[2]	slope: -1.77 $x10^{-3}$ thresh: -0.187
$pcon_{IpvE}$	0.6	[2]	slope: 7.16 $x10^{-3}$ thresh: -1.049	$w_{I5htI5ht,mean}$	-0.37 mV	[2]	slope: -4.12 $x10^{-3}$ thresh: -0.416
$pcon_{IpvIpv}$	0.55	[2]	slope: -2.61 $x10^{-3}$ thresh: -0.0456	$w_{I5htI5ht,median}$	-0.23 mV	[2]	slope: -4.12 $x10^{-3}$ thresh: -0.416
$pcon_{IpvI5ht}$	0.24	[2]	slope: -2.81 $x10^{-3}$ thresh: -0.458	$w_{IsomE,mean}$	-0.5 mV	No data	slope: -0.013 thresh: -0.984
$pcon_{IpvIsom}$	0	No data	Not tested	$w_{IsomE,median}$	-0.4 mV	No data	slope: -0.013 thresh: -0.984

Source [1] is (Lefort et al., 2009), [2] is (Avermann et al., 2012), [3] is (Fanselow et al., 2008), [4] is (Kinnischtzke et al., 2012), [5] is (Fino and Yuste, 2011). *N* is number of neurons, *Vrest* is resting potential, *Vth* is spike voltage threshold, *Rin* is input resistance, *tref* is refractory period, τm is the membrane time constant, τsyn is the synaptic time constant with the first subscript indicating the postsynaptic neuron type and the second subscript the neurotransmitter type of the presynaptic neuron (*e* or *i*), *Erev* is the synaptic reversal potential, *pcon* is the synaptic connection probability, *prel* is the synaptic release probability, *w* is the mean or median post-synaptic potential amplitude as indicated. For all neuronal parameters, the subscript indicates the neuron type: *E* is L2/3 excitatory neurons, *Ipv* is PV neurons, *I5ht* is $5HT_{3A}R$ neurons, *Isom* is SOM neurons, and *EL4* is L4 excitatory neurons. For synaptic parameters, the first and second subscripts indicate the pre- and post-synaptic neuron types, respectively.

Logistic model

From the L2/3 circuit model simulations, we numerically estimated the probability *q* that each neuron in the model fires a spike as a function of the fraction of L4 inputs that were active, *f*.

We then used the generalized linear model regression tool 'glmfit' in MATLAB to find the best fit of the two logistic model parameters for each neuron:

$$q(f) = \frac{1}{1+\exp\left(-\beta(f-f_{1/2})\right)},$$

where the parameter β represents the slope, and the parameter $f_{1/2}$ represents the fraction of active L4 neurons at which the response probability $q = 0.5$. For clarity of presentation, in the main text we converted this $f_{1/2}$ parameter to what we termed the 'threshold', f_{thresh}, which we defined as the fraction of L4 neurons needed to reach a specified spike probability, q_{thresh}. Throughout the study we fixed $q_{thresh} = 0.01$. The threshold is related to $f_{1/2}$ via the inverse of the logistic function

$$f_{thresh} = f_{1/2} + \log\left(\frac{q_{thresh}}{1-q_{thresh}}\right)/\beta.$$

We computed firing rates and pairwise correlations from the logistic model (Figures 3—4) in the following way. First, we assumed that the fraction of active L4 neurons is described by a normally distributed random variable with zero mean and unit variance:

$$p(f) = \frac{\exp\left(-f^2/2\right)}{\sqrt{2\pi}} = \mathcal{N}(0,1).$$

We defined the β and $f_{1/2}$ parameters relative to the mean and standard deviation of the input distribution. Since q is a monotonically increasing function of f, the probability distribution for q is

$$p(q) = p(f(q))\left|\frac{df}{dq}\right|$$

where $f(q)$ is the inverse of the logistic function $q(f)$ and

$\frac{df}{dq} = \frac{\left(\exp\left(-\beta(f-f_{1/2})\right)+1\right)^2}{\beta\exp(-\beta(f-f_{1/2}))}$. We calculate a neuron's mean firing rate μ as the expectation of q,

$$\mu = \mathbb{E}[q] = \int_0^1 [q \times p(q)]dq = \int_0^1 \left[q \times p(f(q))\left|\frac{df}{dq}\right|\right]dq.$$

We calculate the pairwise covariance of two homogeneous neurons driven by a common input f as

$\mathrm{cov} = \mathbb{E}[q^2] - (\mathbb{E}[q])^2 = \mathbb{E}[q^2] - \mu^2 = \int_0^1 \left[q^2 \times p\left(f(q)\right)\left|\frac{df}{dq}\right|\right]dq - \mu^2$, then find the pairwise correlation by normalizing the covariance by the neurons' shared variance, $\mathrm{var} = \mu(1-\mu)$.

For fitting the logistic model to the recorded neural firing rates and correlations (Figure 4), we considered a population model where the joint probability distribution across threshold and slope was specified by a 2D Gaussian, which has five parameters: threshold mean and s.d., slope mean and s.d., and slope-threshold correlation. The three constraint statistics we considered from the neural population data were the mean neural ON probability, the s.d. of neural ON probabilities, and the mean pairwise correlations. We found the best-fit model parameters for each dataset using stochastic gradient descent. We checked for fit convergence by sampling a large number of logistic model parameters from the fitted 2D Gaussian, drawing binary samples from these logistic 'neurons' and computing the ON probability mean and s.d., and mean pairwise correlation from the synthetic binary samples, and comparing the computed statistical values to the original data statistics. For the sensitivity analysis presented in Figure 5, we numerically computed the partial derivative in mean firing rate and pairwise correlation with respect to the mean slope and mean threshold parameters in the population logistical model, using standard finite difference methods.

Statistical tests

To avoid parametric assumptions, all statistical tests were done using standard bootstrapping methods with custom-written MATLAB scripts. For example when assessing the observed difference between two group means $\Delta\mu_{obs}$ we performed the following procedure to calculate a p-value. First we pool the data points from the two groups to create a null set S_{null}. We then construct two hypothetical groups of samples S_1 and S_2 from this by randomly drawing n_1 and n_2 samples with replacement from S_{null}, where n_1 and n_2 are the number of data points in the original groups 1 and 2 respectively. We take the mean of both hypothetical sets $\Delta\mu_1$ and $\Delta\mu_2$ and calculate their difference $\Delta\mu_{null} = \Delta\mu_1 - \Delta\mu_2$. We then repeat the entire procedure 10^7 times to build up a histogram of $\Delta\mu_{null}$. This distribution is always centered at zero. After normalizing, this can be interpreted as the probability distribution $f(\Delta\mu_{null})$ for observing a group mean difference of $\Delta\mu_{null}$ purely by chance if the data were actually sampled from the same null distribution. Then the final p-value for the probability of finding a group difference of at least $\Delta\mu_{obs}$ in either direction is given by $p = \int_{-\infty}^{-\Delta\mu_{obs}} f(\Delta\mu_{null})d\Delta\mu_{null} + \int_{\Delta\mu_{obs}}^{\infty} f(\Delta\mu_{null})d\Delta\mu_{null}$.

Conversion from firing rate to ON/OFF probabilities for Ca^{2+} imaging data

For the Ca^{2+} imaging data, we began with estimated firing rate time series $r_i(t)$ for each neuron *i* recorded as part of a population of *N* neurons. For later parts of the analysis we needed to convert these firing rates to binary ON/OFF values. This conversion involves a choice. One option would be to simply threshold the data, but this would throw away information about the magnitude of the firing rate. We instead take a probabilistic approach where rather than deciding definitively whether a given neuron was ON or OFF in a given time bin, we calculate the probability that the neuron was ON or OFF by assuming that neurons fire action potentials according to an inhomogeneous Poisson process with rate $r_i(t)$. The mean number of spikes $\lambda_i(t)$ expected in a time bin of width Δt is $\lambda_i(t) = r_i(t)\Delta t$. We choose Δt = 1 second. Under the Poisson model the actual number of spikes *m* in a particular time bin is a random variable that follows the Poisson distribution $P(m=k) = \lambda^k \exp(-\lambda) / k!$. We considered a neuron active (ON) if it is firing one or more spikes in a given time bin. Hence the probability that a neuron is ON is $p_{on}(t)=1-P(m=0)=1-\exp(\lambda)$. This approach has two advantages over thresholding: 1) it preserves some information about the magnitude of firing rates, and 2) it acts to regularize the probability distribution for the number of neurons active by essentially smoothing nearby values together.

Entropy estimation for large numbers of neurons

Entropy was estimated by fitting a statistical model we recently developed, called the population tracking model (O'Donnell et al., 2017), to the binarized Ca^{2+} imaging data. Briefly, the population tracking model fits two aspects of the data: the probability distribution for the number of neurons synchronously active in the population, and also the conditional firing probability that each individual neuron is active given the population count. Hence the model captures both some aggregate statistics of the population activity, and some aspects of the heterogeneity across neurons. See O'Donnell et al. (2017) for complete details and validation of the method. Code for fitting the model to data is available at https://github.com/cianodonnell/PopulationTracking.

The entropy/neuron generally decreased with the number of neurons considered as result of the population correlations (Figure 6B), so we needed to control for neural population size

when comparing data from different experimental groups. On the one hand, we would like to study as large a number of neurons as possible, because we expect the effects of collective network dynamics to be stronger for large population sizes and this may be the regime where differences between the groups emerge. On the other hand, our recording methods allowed us to sample only typically around ~100 neurons at a time, and as few as 40 neurons in some animals. Hence we proceeded by first estimating the entropy/neuron in each animal by calculating the entropy of random subsets of neurons of varying size from 10 to 100 (if possible) in steps of 10. For each population size we sampled a large number of independent subsets, calculated the entropy of each. Finally, for each dataset we fit a double exponential function to the estimated entropy/neuron as a function of the number of neurons: $H/N = A^*\exp(-b^*N) + C^*\exp(-d^*N) + e$, and used this fit to estimate H/N for 100 neurons.

Acknowledgements

We thank Timothy O'Leary, Hannes Saal, and Alex Williams for comments on earlier versions of the manuscript. This study was supported by funding from FRAXA Research Foundation, Howard Hughes Medical Institute, Sloan-Swartz Foundation, the Dana Foundation, Developmental Disabilities Translational Research Program grant #20160969 (The John Merck

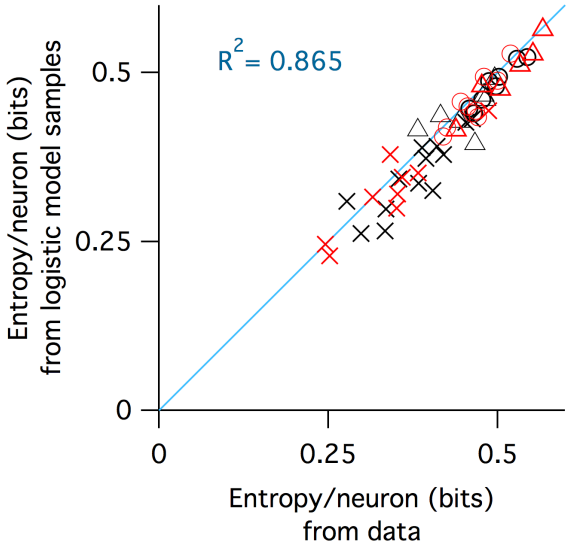

Supp Fig 1. Agreement between entropy estimated from raw data and entropy estimated from samples from fitted logistic models. Black symbols are WT, red are KO. Crosses are P9—11, circles P14—16, triangles P30—40. Blue line is identity, the R^2 value of which is reported in the inset.

612 Fund), SFARI grant 295438 (Simons Foundation) and the NIH (NICHD R01HD054453 and
613 NINDS RC1NS068093).

614 **Competing Interests**

615 The authors have no competing interests to declare.

References

Avermann, M., Tomm, C., Mateo, C., Gerstner, W., Petersen, C.C.H., 2012. Microcircuits of excitatory and inhibitory neurons in layer 2/3 of mouse barrel cortex. J Neurophysiol 107, 3116–3134. doi:10.1152/jn.00917.2011

Bateup, H.S., Takasaki, K.T., Saulnier, J.L., Denefrio, C.L., Sabatini, B.L., 2011. Loss of Tsc1 in vivo impairs hippocampal mGluR-LTD and increases excitatory synaptic function. J Neurosci 31, 8862–8869. doi:10.1523/JNEUROSCI.1617-11.2011

Belmonte, M.K., Allen, G., Beckel-Mitchener, A., Boulanger, L.M., Carper, R.A., Webb, S.J., 2004. Autism and abnormal development of brain connectivity. J Neurosci 24, 9228–9231. doi:10.1523/JNEUROSCI.3340-04.2004

Berkes, P., Orbán, G., Lengyel, M., Fiser, J., 2011. Spontaneous cortical activity reveals hallmarks of an optimal internal model of the environment. Science 331, 83–87. doi:10.1126/science.1195870

Berzhanskaya, J., Phillips, M.A., Shen, J., Colonnese, M.T., 2016. Sensory hypo-excitability in a rat model of fetal development in Fragile X Syndrome. Sci Rep 6, 30769. doi:10.1038/srep30769

Braat, S., Kooy, R.F., 2015. The GABAA Receptor as a Therapeutic Target for Neurodevelopmental Disorders. Neuron 86, 1119–1130. doi:10.1016/j.neuron.2015.03.042

Bureau, I., Shepherd, G.M.G., Svoboda, K., 2008. Circuit and plasticity defects in the developing somatosensory cortex of FMR1 knock-out mice. J Neurosci 28, 5178–5188. doi:10.1523/JNEUROSCI.1076-08.2008

Clancy, K.B., Schnepel, P., Rao, A.T., Feldman, D.E., 2015. Structure of a single whisker representation in layer 2 of mouse somatosensory cortex. J Neurosci 35, 3946–3958. doi:10.1523/JNEUROSCI.3887-14.2015

Contractor, A., Klyachko, V.A., Portera-Cailliau, C., 2015. Altered Neuronal and Circuit Excitability in Fragile X Syndrome. Neuron 87, 699–715. doi:10.1016/j.neuron.2015.06.017

Cover, T.M., Thomas, J.A., 2006. Elements of Information Theory, 2nd ed. Wiley-Interscience.

Cruz-Martin, A., Crespo, M., Portera-Cailliau, C., 2010. Delayed Stabilization of Dendritic Spines in Fragile X Mice. J Neurosci 30, 7793–7803. doi:10.1523/JNEUROSCI.0577-10.2010

Dani, V.S., Chang, Q., Maffei, A., Turrigiano, G.G., Jaenisch, R., Nelson, S.B., 2005. Reduced cortical activity due to a shift in the balance between excitation and inhibition in a mouse model of Rett syndrome. Proc. Natl. Acad. Sci. U.S.A. 102, 12560–12565. doi:10.1073/pnas.0506071102

Fanselow, E.E., Richardson, K.A., Connors, B.W., 2008. Selective, state-dependent activation of somatostatin-expressing inhibitory interneurons in mouse neocortex. J Neurophysiol 100, 2640–2652. doi:10.1152/jn.90691.2008

Fino, E., Yuste, R., 2011. Dense inhibitory connectivity in neocortex. Neuron 69, 1188–1203. doi:10.1016/j.neuron.2011.02.025

Frye, C.G., Maclean, J.N., 2016. Spontaneous activations follow a common developmental course across primary sensory areas in mouse neocortex. J Neurophysiol 116, 431–437. doi:10.1152/jn.00172.2016

Gentet, L.J., Kremer, Y., Taniguchi, H., Huang, Z.J., Staiger, J.F., Petersen, C.C.H., 2012.

659 Unique functional properties of somatostatin-expressing GABAergic neurons in mouse
660 barrel cortex. Nat Neurosci 15, 607–612. doi:10.1038/nn.3051
661 Gibson, J.R., Bartley, A.F., Hays, S.A., Huber, K.M., 2008. Imbalance of neocortical excitation
662 and inhibition and altered UP states reflect network hyperexcitability in the mouse model of
663 fragile X syndrome. J Neurophysiol 100, 2615–2626. doi:10.1152/jn.90752.2008
664 Golshani, P., Gonçalves, J.T., Khoshkhoo, S., Mostany, R., Smirnakis, S., Portera-Cailliau, C.,
665 2009. Internally mediated developmental desynchronization of neocortical network activity.
666 J Neurosci 29, 10890–10899. doi:10.1523/JNEUROSCI.2012-09.2009
667 Gonçalves, J.T., Anstey, J.E., Golshani, P., Portera-Cailliau, C., 2013. Circuit level defects in
668 the developing neocortex of Fragile X mice. Nat Neurosci 16, 903–909.
669 doi:10.1038/nn.3415
670 Goodman, D.F.M., Brette, R., 2009. The brian simulator. Front Neurosci 3, 192–197.
671 doi:10.3389/neuro.01.026.2009
672 Gutenkunst, R.N., Waterfall, J.J., Casey, F.P., Brown, K.S., Myers, C.R., Sethna, J.P., 2007.
673 Universally sloppy parameter sensitivities in systems biology models. PLoS Comput Biol 3,
674 1871–1878. doi:10.1371/journal.pcbi.0030189
675 Harlow, E.G., Till, S.M., Russell, T.A., Wijetunge, L.S., Kind, P., Contractor, A., 2010. Critical
676 period plasticity is disrupted in the barrel cortex of FMR1 knockout mice. Neuron 65, 385–
677 398. doi:10.1016/j.neuron.2010.01.024
678 Hays, S.A., Huber, K.M., Gibson, J.R., 2011. Altered neocortical rhythmic activity states in
679 Fmr1 KO mice are due to enhanced mGluR5 signaling and involve changes in excitatory
680 circuitry. J Neurosci 31, 14223–14234. doi:10.1523/JNEUROSCI.3157-11.2011
681 He, Q., Nomura, T., Xu, J., Contractor, A., 2014. The developmental switch in GABA polarity is
682 delayed in fragile X mice. J Neurosci 34, 446–450. doi:10.1523/JNEUROSCI.4447-13.2014
683 Kehrer, C., Maziashvili, N., Dugladze, T., Gloveli, T., 2008. Altered Excitatory-Inhibitory
684 Balance in the NMDA-Hypofunction Model of Schizophrenia. Frontiers in Molecular
685 Neuroscience 1, 6. doi:10.3389/neuro.02.006.2008
686 Kerr, J.N.D., de Kock, C.P.J., Greenberg, D.S., Bruno, R.M., Sakmann, B., Helmchen, F., 2007.
687 Spatial organization of neuronal population responses in layer 2/3 of rat barrel cortex. J
688 Neurosci 27, 13316–13328. doi:10.1523/JNEUROSCI.2210-07.2007
689 Kinnischtzke, A.K., Sewall, A.M., Berkepile, J.M., Fanselow, E.E., 2012. Postnatal maturation
690 of somatostatin-expressing inhibitory cells in the somatosensory cortex of GIN mice. Front
691 Neural Circuits 6, 33. doi:10.3389/fncir.2012.00033
692 La Fata, G., Gärtner, A., Domínguez-Iturza, N., Dresselaers, T., Dawitz, J., Poorthuis, R.B.,
693 Averna, M., Himmelreich, U., Meredith, R.M., Achsel, T., Dotti, C.G., Bagni, C., 2014.
694 FMRP regulates multipolar to bipolar transition affecting neuronal migration and cortical
695 circuitry. Nat Neurosci. doi:10.1038/nn.3870
696 Lefort, S., Tomm, C., Floyd Sarria, J.-C., Petersen, C.C.H., 2009. The excitatory neuronal
697 network of the C2 barrel column in mouse primary somatosensory cortex. Neuron 61, 301–
698 316. doi:10.1016/j.neuron.2008.12.020
699 Lu, H., Ash, R.T., He, L., Kee, S.E., Wang, W., Yu, D., Hao, S., Meng, X., Ure, K., Ito-Ishida, A.,
700 Tang, B., Sun, Y., Ji, D., Tang, J., Arenkiel, B.R., Smirnakis, S.M., Zoghbi, H.Y., 2016.
701 Loss and Gain of MeCP2 Cause Similar Hippocampal Circuit Dysfunction that Is Rescued
702 by Deep Brain Stimulation in a Rett Syndrome Mouse Model. Neuron 91, 739–747.

doi:10.1016/j.neuron.2016.07.018

Luczak, A., Bartho, P., Harris, K.D., 2009. Spontaneous events outline the realm of possible sensory responses in neocortical populations. Neuron 62, 413–425. doi:10.1016/j.neuron.2009.03.014

Mao, T., Kusefoglu, D., Hooks, B.M., Huber, D., Petreanu, L., Svoboda, K., 2011. Long-range neuronal circuits underlying the interaction between sensory and motor cortex. Neuron 72, 111–123. doi:10.1016/j.neuron.2011.07.029

Meredith, R.M., Dawitz, J., Kramvis, I., 2012. Sensitive time-windows for susceptibility in neurodevelopmental disorders. Trends Neurosci 35, 335–344. doi:10.1016/j.tins.2012.03.005

Miller, J.-E.K., Ayzenshtat, I., Carrillo-Reid, L., Yuste, R., 2014. Visual stimuli recruit intrinsically generated cortical ensembles. 111, E4053–E4061. doi:10.1073/pnas.1406077111

Mitra, A., Snyder, A.Z., Blazey, T., Raichle, M.E., 2015. Lag threads organize the brain's intrinsic activity. Proc. Natl. Acad. Sci. U.S.A. 112, E2235–E2244. doi:10.1073/pnas.1503960112

O'Donnell, C., Gonçalves, J.T., Whiteley, N., Portera-Cailliau, C., Sejnowski, T.J., 2017. The Population Tracking Model: A Simple, Scalable Statistical Model for Neural Population Data. Neural Comput 29, 50–93. doi:10.1162/NECO_a_00910

O'Leary, T., Sutton, A.C., Marder, E., 2015. Computational models in the age of large datasets. Curr Opin Neurobiol 32C, 87–94. doi:10.1016/j.conb.2015.01.006

Paluszkiewicz, S.M., Olmos-Serrano, J.L., Corbin, J.G., Huntsman, M.M., 2011. Impaired inhibitory control of cortical synchronization in fragile X syndrome. J Neurophysiol 106, 2264–2272. doi:10.1152/jn.00421.2011

Patel, A.B., Hays, S.A., Bureau, I., Huber, K.M., Gibson, J.R., 2013. A target cell-specific role for presynaptic Fmr1 in regulating glutamate release onto neocortical fast-spiking inhibitory neurons. J Neurosci 33, 2593–2604. doi:10.1523/JNEUROSCI.2447-12.2013

Petersen, C.C.H., Crochet, S., 2013. Synaptic computation and sensory processing in neocortical layer 2/3. Neuron 78, 28–48. doi:10.1016/j.neuron.2013.03.020

Petreanu, L., Huber, D., Sobczyk, A., Svoboda, K., 2007. Channelrhodopsin-2-assisted circuit mapping of long-range callosal projections., Nature neuroscience. doi:10.1038/nn1891

Pologruto, T.A., Yasuda, R., Svoboda, K., 2004. Monitoring neural activity and [Ca2+] with genetically encoded Ca2+ indicators. J Neurosci 24, 9572–9579. doi:10.1523/JNEUROSCI.2854-04.2004

Qian, N., Lipkin, R.M., 2011. A learning-style theory for understanding autistic behaviors. Front Hum Neurosci 5, 77. doi:10.3389/fnhum.2011.00077

Quian Quiroga, R., Panzeri, S., 2009. Extracting information from neuronal populations: information theory and decoding approaches. Nat Rev Neurosci 10, 173–185. doi:10.1038/nrn2578

Ringach, D.L., 2009. Spontaneous and driven cortical activity: implications for computation. Curr Opin Neurobiol 19, 439–444. doi:10.1016/j.conb.2009.07.005

Rochefort, N.L., Garaschuk, O., Milos, R.-I., Narushima, M., Marandi, N., Pichler, B., Kovalchuk, Y., Konnerth, A., 2009. Sparsification of neuronal activity in the visual cortex at eye-opening. 106, 15049–15054. doi:10.1073/pnas.0907660106

747 Rubenstein, J.L.R., Merzenich, M.M., 2003. Model of autism: increased ratio of
748 excitation/inhibition in key neural systems. Genes Brain Behav. 2, 255–267.
749 Sato, T.R., Gray, N.W., Mainen, Z.F., Svoboda, K., 2007. The functional microarchitecture of
750 the mouse barrel cortex. PLoS Biol 5, e189. doi:10.1371/journal.pbio.0050189
751 Schneidman, E., Berry, M.J., Segev, R., Bialek, W., 2006. Weak pairwise correlations imply
752 strongly correlated network states in a neural population. Nature 440, 1007–1012.
753 doi:10.1038/nature04701
754 Selby, L., Zhang, C., Sun, Q.-Q., 2007. Major defects in neocortical GABAergic inhibitory
755 circuits in mice lacking the fragile X mental retardation protein. Neurosci. Lett. 412, 227–
756 232. doi:10.1016/j.neulet.2006.11.062
757 Testa-Silva, G., Loebel, A., Giugliano, M., de Kock, C.P.J., Mansvelder, H.D., Meredith, R.M.,
758 2012. Hyperconnectivity and slow synapses during early development of medial prefrontal
759 cortex in a mouse model for mental retardation and autism. Cereb Cortex 22, 1333–1342.
760 doi:10.1093/cercor/bhr224
761 Tomm, C., Avermann, M., Petersen, C., Gerstner, W., Vogels, T.P., 2014. Connection-type-
762 specific biases make uniform random network models consistent with cortical recordings. J
763 Neurophysiol 112, 1801–1814. doi:10.1152/jn.00629.2013
764 Wallace, M.L., Burette, A.C., Weinberg, R.J., Philpot, B.D., 2012. Maternal loss of Ube3a
765 produces an excitatory/inhibitory imbalance through neuron type-specific synaptic defects.
766 Neuron 74, 793–800. doi:10.1016/j.neuron.2012.03.036
767 Yaksi, E., Friedrich, R.W., 2006. Reconstruction of firing rate changes across neuronal
768 populations by temporally deconvolved Ca2+ imaging. Nat. Methods 3, 377–383.
769 doi:10.1038/nmeth874
770